Thickness-Dependent Charge Transport in Three Dimensional Ru(II)− Tris(phenanthroline)-Based Molecular Assemblies

Ritu Gupta, Shapath Bhandari, Savas Kaya, Konstantin P. Katin, and Prakash Chandra Mondal*

ACCESS | Metrics & More | Article Recommendations | Supporting Information

ABSTRACT: We describe here the fabrication of large-area molecular junctions with a configuration of ITO/[Ru(Phen)$_3$]/Al to understand temperature- and thickness-dependent charge transport phenomena. Thanks to the electrochemical technique, thin layers of electroactive ruthenium(II)−tris(phenanthroline) [Ru(Phen)$_3$] with thicknesses of 4−16 nm are covalently grown on sputtering-deposited patterned ITO electrodes. The bias-induced molecular junctions exhibit symmetric current−voltage (j−V) curves, demonstrating highly efficient long-range charge transport and weak attenuation with increased molecular film thickness (β = 0.70 to 0.79 nm^{-1}). Such a lower β value is attributed to the accessibility of Ru(Phen)$_3$ molecular conduction channels to Fermi levels of both the electrodes and a strong electronic coupling at ITO− molecules interfaces. The thinner junctions (d = 3.9 nm) follow charge transport via resonant tunneling, while the thicker junctions (d = 10−16 nm) follow thermally activated (activation energy, E$_a$ ~ 43 meV) Poole−Frenkel charge conduction, showing a clear "molecular signature" in the nanometric junctions.

KEYWORDS: electrosynthesis, 3-dimensional network, crossbar junctions, electric field, charge transport
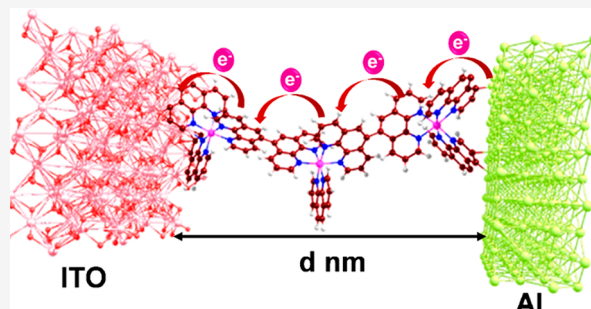
The prime core of molecular electronics is to cognize and understand charge transport mechanisms at nanoscale molecular junctions (MJs) with varied molecular structures, compositions, electrode combinations, and device stacking platforms.[1−4] Toward this goal, a forward-looking approach is to assemble either a single molecule or a few molecules between two electrical conductors, which is popularly known as molecular electronics.[5−8] Charge conduction in response to an applied external bias to MJs with a conventional device stacking, metal/molecules/metal, can be influenced by various factors.[9−13] The factors include electronic coupling to the electrode/molecule(s) interfaces, electrode composition, Fermi energy, the thickness of the molecular layers, packing and orientation on the electrode surface, and frontier molecular orbital energies governing charge transport phenomena.[14−18] Significant progress has been made with MJs consisting of organic molecules as test beds to understand charge transport characteristics.[19−21] The redox-active MJs containing metal centers with an extended π-conjugated backbone can exhibit long-range charge transport due to relatively less band gap between the highest occupied molecular orbital (HOMO) and lowest unoccupied molecular orbital (LUMO) and involvement of redox centers. As a result, their current−voltage response is almost independent of length, thus yielding low attenuation factors.[22,23] Ruthenium−polypyridyl complexes are considered model systems for investigating photophysical studies and finding wider applications in redox, catalytic, sensing, and biological

properties.[24−27] However, not much work is reported with ruthenium−polypyridyls in MJs for understanding charge transport across the films with varied structures, configurations, and compositions.[28−31] Besides, many reports focus on thiolated self-assembled monolayers (SAMs), silane-based coupling layers, phosphonic linkers, or single and bis-aryl diazonium salts for electrochemically (E-Chem) grafting the molecular layer on the various electrodes ranging from Au, doped Si, Cu, Co, Ni, ITO, and carbon contacts.[32−34] An electrochemical reduction method in creating faster molecular layers of diverse structures, composition, and desired thickness is advantageous as the process happens via forming radicals near the working electrode surface via electroreduction of aryl diazonium salts.[35−38]

Among the various molecular layers, three-dimensional (3D) coordination-based molecular assemblies offer fascinating features, including optical, redox, electrochromic, logic-gate, and linear vs exponential film growth and are mostly grown via the layer-by-layer (LbL) method using stepwise coordination between metal ions and organic linkers.[27,39,40] Incorporating
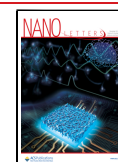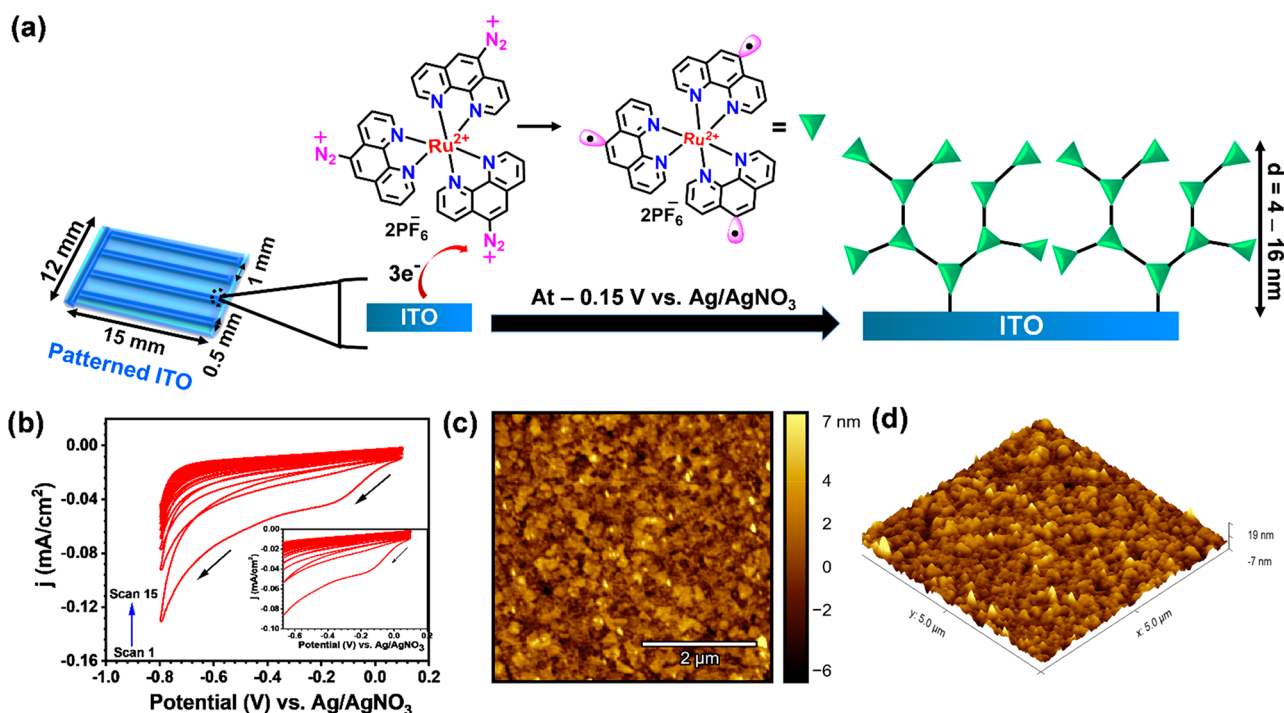
Figure 1. (a) Proposed schematic of electrochemical (E-Chem) grafting of in situ generated diazonium salts of $Ru(Phen)_3 \cdot 2PF_6$ on a patterned ITO electrode, (b) cyclic voltammograms of E-Chem reduction recorded at 100 mV s^{-1} up to 15 scans, and (c, d) noncontact mode 2D and 3D AFM images of $Ru(Phen)_3$ thin film on ITO, respectively.
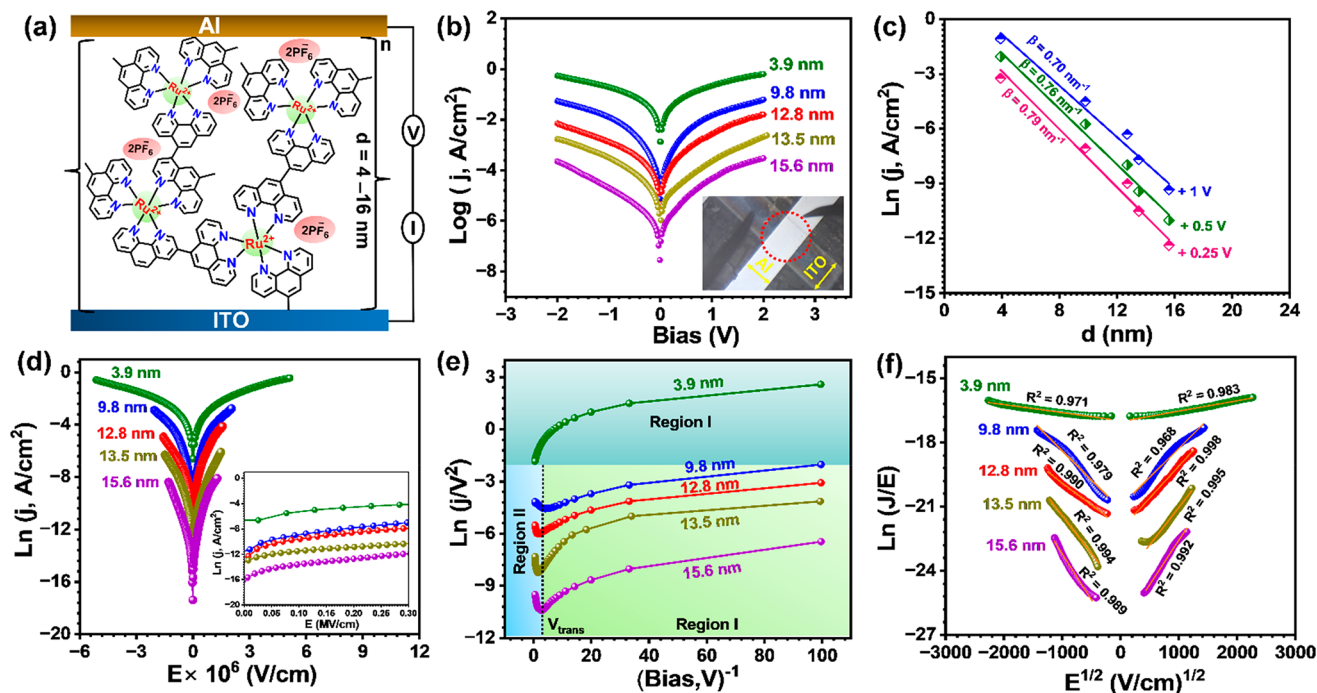
Figure 2. (a) Side view of two-terminal MJs with vertical stacking of $ITO/[Ru(Phen)_3]_{d=4-16 \text{ nm}}/Al$, (b) Semilog j−V curves for $Ru(Phen)_3$ MJs with the molecular thickness of 4−16 nm (inset showing an image of MJ). The j−V curves are the average of 6−7 individual MJs. (c) ln j vs d plot at different biases for estimating β values, (d) comparison of ln j vs E plot for different thicknesses of $Ru(Phen)_3$ MJs, and (e) FN plot and (f) PF plot for different thicknesses of $Ru(Phen)_3$ MJs.

such 3D molecular assemblies where more redox centers are accumulated in an MJ for understanding charge transport at systematic layer thickness variation would help mimic conventional electronic functions. The present work deals with $Ru(Phen)_3 \cdot 2PF_6$ as an active circuit element grown in a three-dimensional (3D) architecture on patterned ITO followed by an Al top contact deposition. We have chosen a popular ligand framework, which is 1,10-phenanthroline (or simply Phen), very similar to bidentate chelating ligand 2,2′-bipyridine for coordinating it with Ru(II) and synthesized
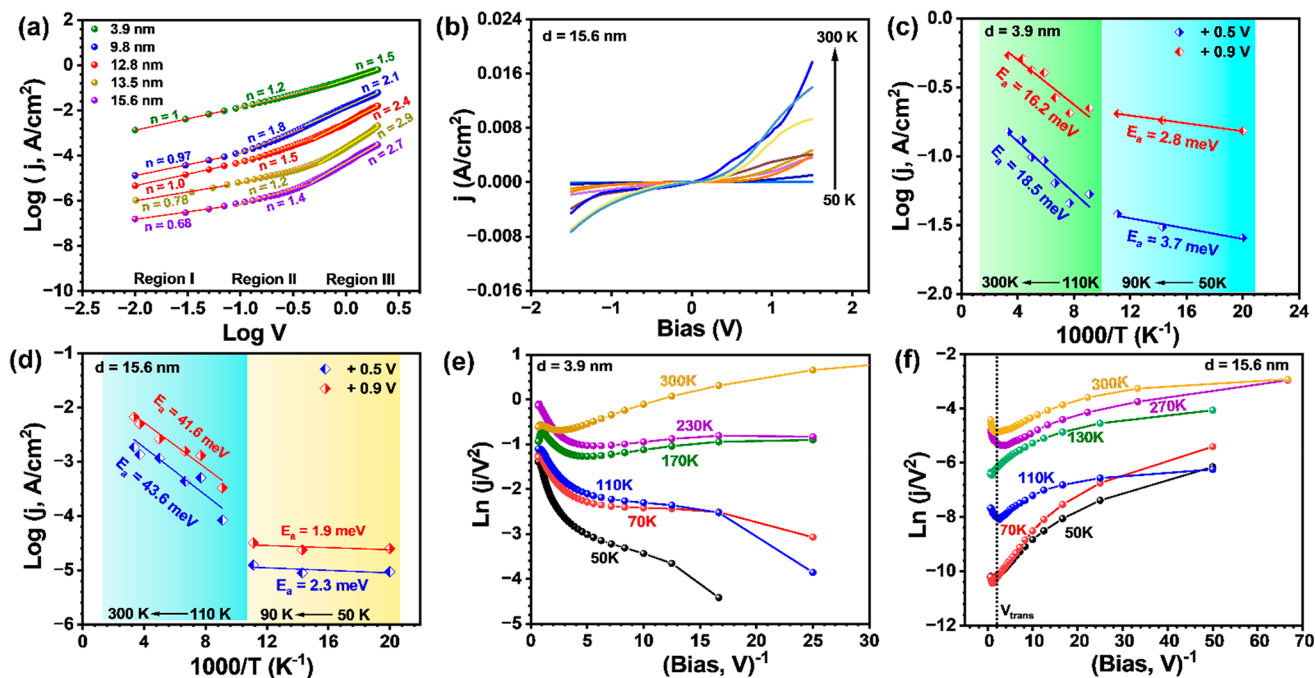
Figure 3. (a) Plots of log j vs log V for MJs for different thicknesses of Ru(Phen)$_3$ MJs in a positive potential window. (b) j−V curves for d = 3.9 nm MJs plotted from 50 to 300 K. (c) Arrhenius curves for d = 3.9 nm MJs and (d) for d = 15.6 nm MJs. (e) FN plot for d = 3.9 nm MJs and (f) for d = 15.6 nm MJs recorded at different temperatures.

complex bearing three 5-amino-1,10-phenanthroline (Figures S1−S10). The current study was motivated to understand charge transport beyond the tunneling regime (d > 5 nm) in 3D-grown Ru(Phen)$_3$ layers, particularly in the role of structures and orbital energies.

The diazonium salts are formed in situ by the addition of t-butylnitrite (^{t}BuNO$_2$) to the Ru(II)-complex. The electrochemical reduction of tris-diazonium generates radicals at three different sites, facilitating the three-dimensional growth of Ru(Phen)$_3$ oligomers (Figure 1a). During the first voltammogram scan, a broad irreversible reduction peak appears at −0.15 V vs Ag/AgNO$_3$, characteristics of diazonium reduction to radicals. In the next CV cycles, a decrease in the reduction current density was noted (Figure 1b). Ultrathin Ru(Phen)$_3$ films with thickness from 4 to 16 nm are formed by the varying potential window and number of CV scans, and their thickness measurements are performed via atomic force microscopy (AFM) measurements (Figures S11−S14, Table S1). A clear, well-ordered grain structure of the Ru(Phen)$_3$ film across the surface is observed (Figure 1c,d). The root-mean-square (RMS) roughness of the Ru(Phen)$_3$ thin film was ∼2.5 nm, slightly higher than that of bare ITO (RMS roughness = 2.3 nm). The UV−vis absorbance spectra of the thin films show two signals, one at 365 nm and the other at 570 nm, corresponding to π−π* transition and metal-to-ligand charge transfer band, respectively, ensuring the growth of molecular layers on ITO surfaces (Figure S15).[41] Moreover, the anchorage of the Ru(Phen)$_3$ thin films on the ITO substrate was estimated by cyclic voltammetry (CV). The CV curve shows a characteristic one electron oxidation peak due to Ru(II) to Ru(III) forming at +1.36 V vs Ag/AgNO$_3$ and a redox-peak due to Ru(III) to Ru(II) at +1.08 V vs Ag/AgNO$_3$, which matches well with the previous literature (Figure S16a).[41] The cathodic potentials at −1.04 and −1.40 V vs Ag/AgNO$_3$ are attributed to ligand-based one electron

reduction phenomena (Figure S16b). In addition, X-ray photoelectron spectroscopy (XPS) survey spectra confirm all the expected elements peaks, including C 1s, Ru 3d, O 1s, N 1s, F 1s, and P 2p for Ru(Phen)$_3$ layer growth (Figures S17 and S18a). The XPS spectrum shows a characteristic peak at 280 eV assigned to the Ru(II) 3d$_{5/2}$, while the Ru(II) 3d$_{3/2}$ signal is masked under the C 1s peak (Figure S18b), which is also a common feature.[28] The detailed XPS results are discussed in the Supporting Information (Figure S18c,d, Table S2).

A top Al electrode of ∼50 nm was deposited by thermal evaporation (the chamber base pressure was maintained at 5 × 10^{-6} mbar, deposition rate was of 0.2−0.3 Å/s) to complete the molecular junctions (Figures 2a and S19−20). The room-temperature current density (A/cm^2) vs bias (j−V) plots for several Ru(Phen)$_3$ MJs with five different molecular layer thicknesses in the range of d = 4 16 nm are shown in Figures S21−25. The yield of the working junctions was quite high (>91%, 11 out of 12 junctions), illuminating the potential of diazonium-based MJs for real applications (Table S3). Figure 2b shows overlays of the semilog j−V plot for Ru(Phen)$_3$ MJs (average of 6−7 individual MJs measurements). The difference in current density (j) by the orders of magnitude for each thickness of Ru(Phen)$_3$ oligomers clearly depicts the dependence of the electrical properties on the molecular lengths. Such a "thickness signature" plays a crucial role in governing the charge conduction phenomena in molecular electronics. The linear dependence of ln j with molecular thickness (d) from 4 to 16 nm at a particular bias indicates that the simplified Simmons equation 1 applies over such a large thickness range, which suggests that the tunneling current decreases exponentially with the molecular thickness. Here, j is the current density at a particular bias, and β is the tunneling attenuation factor.[42]
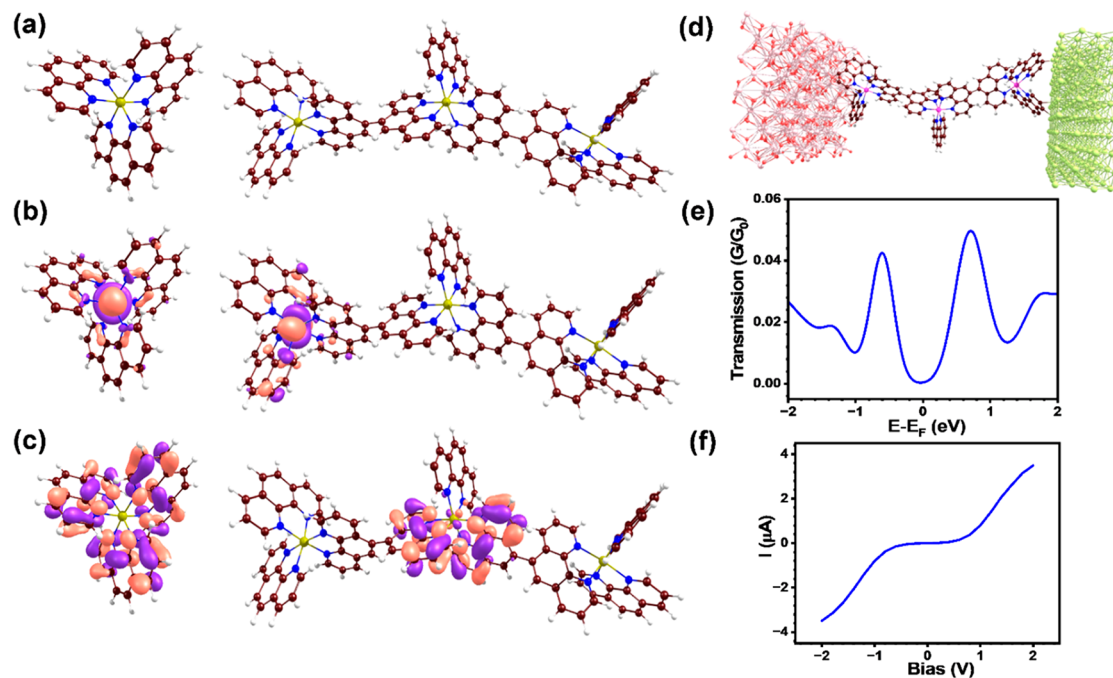
Figure 4. Molecular structure of the (a) HOMO, (b) LUMO, and (c) orbitals of the $(Ru(Phen)_3)^{2+}$ (left) and $(Ru[Phen]_3)_3^{6+}$ (right) complexes. (d) Atomistic model of the considered molecular junction. The $(Ru[ligand]_3)_3^{6+}$ complex connects the ITO lead (left) with the aluminum lead (right). (e) Transmission and (f) I−V characteristics of the considered molecular junction.

$$j = j_0 e^{-\beta d} \tag{1}$$

At V = +0.25 and +0.5 V, the β values were found to be 0.79 nm^{-1} and 0.76 nm^{-1}, respectively, which decreased to 0.70 nm^{-1} at +1 V bias, thus fitting in the desired range of redox-active MJs and demonstrating the highly efficient long-range charge conduction (Figure 2c). A similar range β value is also reported for MJs of Ru(II)−polypyridyl, but at a relatively higher bias = +3 V.[28] The plots of the conductance (dj/dV) vs bias (V) are made to illustrate the local density of states (LDOS) for all five different thicknesses of the MJs (Figures S26−30), suggesting that the molecular orbitals effectively participate in the charge conduction. Various experimental conditions, such as applied bias, electric field, barrier height, and temperature, can be considered to elucidate the long-range charge mechanism. We carefully examined the electric field (E) dependence on the j−V characteristics of Ru(Phen)$_3$ junctions for d = 4−16 nm (Figure 2d). As "d" increases from 3.9 nm, the ln j vs E curve begins to superimpose slightly, suggesting that charge transport may occur through the E-field dependent for the thicker junctions.[43] A similar observation was made with bisthienylbenzene (BTB) and Ru(bpy)$_3$ based MJs.[29,43] A thickness-dependent charge transport regime is obtained in the Fowler-Nordheim (FN) plot. At low bias, linear tunneling behavior follows the Simmons model, equation S1. At high applied bias, the tunneling barrier shape changes from trapezoidal to triangular, and the system adapts to the FN (field-emission) model, equation S3. The change in the mechanism to field emission for thicker (d = 9.8−15.6 nm) Ru(Phen)$_3$ MJs is clearly visible in Figure 2e. At low bias (region I), the current density logarithmically scales with V^{-1}, indicating a direct tunneling mechanism. Above the transition voltage (V_{trans}), current density scales linearly with V^{-1} (region II), characteristics of field emission (equation S2). V_{trans} for different thicknesses are compared in Table S4. However, no

such transition is observed for the thin (d = 3.9 nm) MJs, illustrating direct tunneling as a key charge transport route. The Pool−Frenkel (PF) charge transport mechanism is expected to show a linear plot of ln(j/E) vs $E^{1/2}$; similar curves are shown in Figure 2f.[44] It describes a thermal escape of charge from one trap site to another at a high applied electric field when the potential wall of one trap site is moved down due to a high E-field. The 4−10 nm thick MJs showed a less linear fit with an R^2 value of ~0.978, indicating weak E-field dependence. However, the 10−16 nm junctions show excellent linearity with a R^2 = 0.998. The results from both FN and PF plots support E-field-driven charge conduction in the thicker Ru(Phen)$_3$ MJs. The log j vs log V curve was plotted from average j−V plots for all thicknesses, which shows three regions with varying slopes (n) (Figures 3a and S31). At low bias in region I, the number of injected charge carriers did not exceed the free thermal charge carriers, thus following the linear behavior with a slope n = ~1 for all thickness ranges. At higher bias in regions I and II, a major departure from the linear behavior was obtained for thicker junction well-matches with the FN model (Tables S5−S6).[45]

Figure 3b shows j−V curves obtained from 50 to 300 K for Ru(Phen)$_3$ MJs with d = 15.6 nm. The j−V curves for d = 3.9 nm MJs at a similar temperature range are provided in Figure S32. Importantly, for d = 3.9 nm, the current magnitude was weakly dependent on temperature compared to that of d = 15.6 nm MJs. Next, Arrhenius curves are derived from these j−V plots at two bias values, and slopes provide activation barrier energy (E_a) (Figure 3c,d).[29,46] The results indicate quite low activation energy (E_a ~ 18 meV) for d = 3.9 nm MJs at a high-temperature range (110−300 K), hence consistent with the resonant tunneling mechanism. For thicker MJs (d = 15.6 nm), there is an additional activated mechanism involved at a high-temperature range (E_a ~ 43 meV), suggesting that on-resonant may not only be the mechanism; in contrast, it is at low
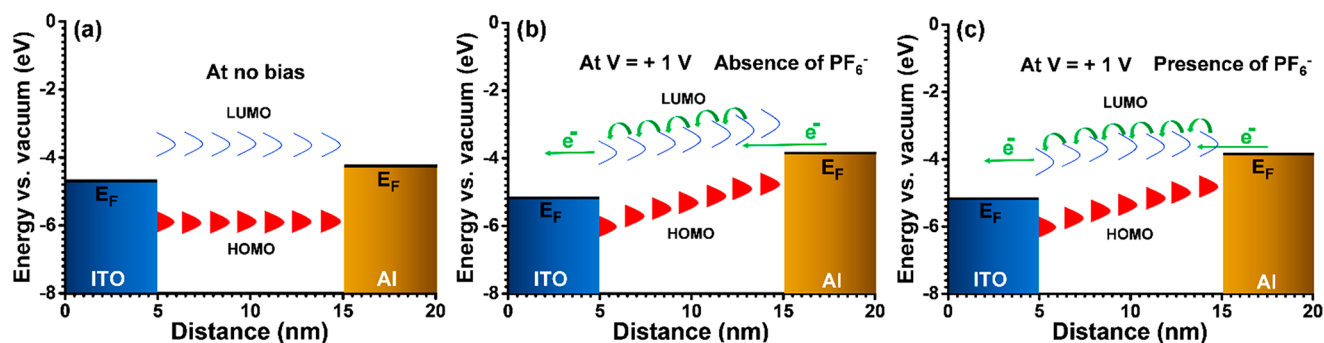
Figure 5. Energy profile for ITO/Ru(Phen)$_3$/Al MJs in the connected state (a) at no bias, (b) at +1 V bias, and (c) at +1 V in the presence of PF$_6^-$ counterions.

temperature (E$_a$ ∼ 2 meV). Additionally, the linear region in the FN plot at all temperature ranges for thicker junctions (d = 15.6 nm) suggests the change in the mechanism from tunneling to field emission. However, the FN plot does not obey the thinnest Ru(Phen)$_3$ MJs (Figure 3e,f).

Similarly, the excellent linearity of ln(j/E) vs E$^{1/2}$, for the d = 15.6 nm junction, especially at high temperatures, signifies that the PF mechanism may be valid and is consistent at all temperatures, which was lacking in d = 3.9 nm MJs (Figures S33 and 34). Moreover, electrical impedance spectroscopy (EIS) studies are performed with the MJs to determine individual electrical parameters, such as contact resistance, capacitance, and charge transfer resistance, which are highly desirable parameters for practical applications.[47] A Nyquist plot shows a single depressed semicircle, indicating one capacitor (Figure S35). With an increase in the thickness of the Ru(Phen)$_3$ layers, the diameter of the semicircle also increases linearly, suggesting an increase in charge transfer resistance (R$_{ct}$). A similar observation can also be seen in the Bode plot (Figure S36). The experimental data are modeled using a modified Randles circuit (Section 17, Figure S37). To further strengthen our insight into the charge transport phenomena, a computational study was carried out with (Ru(Phen)$_3$)$^{2+}$ and its trimer (Ru(Phen)$_3$)$_3^{6+}$ (Figure 4a−c, Figure S38). The HOMO is located mostly on metal ions, whereas the LUMO is distributed on the ligands. Calculated HOMO−LUMO gaps are equal to 3.64 and 2.66 eV for (Ru(Phen)$_3$)$^{2+}$ and (Ru(Phen)$_3$)$_3^{6+}$, respectively. Reducing the width of the HOMO−LUMO gap during the transition from a monomer to a polymer is a common effect. In the trimer, three orbitals of similar energy appear, each localized mainly on one of the ruthenium(II) ions. One such orbital is the HOMO for the trimer. The UV absorbance spectra are provided in Figure S39, and excitation energies corresponding to oscillator strengths are shown in Table S8. The main excitation energy of (Ru(Phen)$_3$)$_3^{6+}$ (364.9 nm) is in good agreement with the experimentally observed absorption at 365 nm. Transport properties of the (Ru(Phen)$_3$)$_3^{6+}$ complex were defined with the DFT combined with the nonequilibrium Green function approach.[48,49] The left lead, ITO, was simulated with the In$_{28}$Sn$_4$O$_{48}$ cubic cell with the equilibrium lattice parameter a$_1$ = 1.030 nm.[50] The right aluminum lead was simulated with the Al$_4$ cubic cell with the equilibrium lattice parameter a$_2$ = 0.405 nm. The scattering region was represented by a complex system, including 2 × 2 × 1 left lead cells and 5 × 5 × 1 right lead cells connected by (Ru(Phen)$_3$)$_3^{6+}$(Figure 4d). Such a molecular thin film orientation could be one of the possibilities. The transmission function is shown in Figure

4e. The I−V curve presented in Figure 4f was calculated at temperature T = 300 K from the transmission with the Landauer−Buttiker formula.[51]

$$I = \frac{2e}{h} \int_{-\infty}^{\infty} T(E)(F(E - 0.5 \text{ eV}) - F(E + 0.5 \text{ eV})) \, dE \tag{2}$$

Here e and h are the elementary charge and the Plank constant, respectively, and F(x) = 1/(1 + exp(x/kT)) is the Fermi−Dirac distribution function. The transmission at the Fermi level is low because it lies inside the gap of the molecule (Figure 4e). Two peaks on the T(E) plot show that, at the energy, which is about 0.8 eV lower/higher than the Fermi level, the transmission is more probable due to resonance tunneling through HOMO/LUMO orbitals. These peaks are the origin of the nonlinear I−V characteristic above ±0.75 V presented in Figure 4f. It demonstrates a significant increase in the slope when the absolute value of V achieves about 0.8 eV.

Based on experimental and theoretical shreds of evidence, a plausible energy diagram for Ru(Phen)$_3$ MJs is depicted (Figure 5). Considering the thickness of the single molecular unit, approximately 1.3 nm (Figure S40), seven repeating units are placed (for 10 nm thick oligomer films) between two electrodes. From the optical and electrochemical thin film data, HOMO and LUMO were estimated to be around −5.62 and −3.98 eV with a band gap of 1.64 eV (see Section 15), while the E$_F$ values of ITO and Al are −4.7 and −4.3 eV, respectively. Due to the strong covalent bonding of Ru(Phen)$_3$ with the ITO electrode, we infer strong electronic coupling at the ITO/Ru(Phen)$_3$ interface. Hence, the LUMO of the Ru(Phen)$_3$ layer is expected to be pinned to the electrode and considerably broadened, as shown in Figure 5a, at no bias condition. Since the LUMO energy for the Ru(Phen)$_3$ layer is near the Fermi (E$_F$) level of the electrodes, the LUMO-mediated electron-driven charge transport is expected here (Figure 5b). When a bias is applied (irrespective of bias polarity), electrons can easily be injected into the layers, because there will always be molecular levels in resonance with the Fermi level of any of the electrodes. Thus, it will provide high current density between the electrodes with no preferred direction (no rectification) and hence a low β value. FN plot, PF plot, and temperature-dependent j−V characteristics also support the resonant tunneling in thinner MJs. In contrast, the classical field-assisted activation (PF) mechanism is expected for thicker MJs. Also, negatively charged PF$_6^-$ ions are present in the film that can interact with the positively biased electrode surface; thus, the potential profile might shift from the ideal linearity (Figure 5c).

In conclusion, we present electrochemically grafted nanometric Ru(Phen)$_3$ molecular layers for the fabrication of molecular junctions to understand the charge transport mechanism in various thicknesses of molecular films. The electrode−molecule interfaces yield covalent bonds, which is crucial in the context of the device's integrity, reproducibility, high yield, and stability. A covalent interface minimizes voltage loss; thus, the junctions can show a maximum output. The electrochemical method also helps to acquire compact and nearly 'pinhole-free' layers, thus suppressing the metal atom penetration during a top contact deposition; therefore, one can achieve high-yield devices (>90%, Table S6). The redox-active Ru(Phen)$_3$ molecular junctions show long-range charge conduction, very similar to a "conducting wire", with a low attenuation factor of 0.70 nm^{-1}. We observe distinct charge conduction mechanisms with thinner compared to thicker junctions (tunneling vs E-field-dependent). Experimental outcomes indicate thermally activated (E$_a$ ∼ 43 meV) Pool−Frenkel as a dominant charge transport mechanism for thicker junctions. In conjunction with the electric field, such energy pushes the charge carriers to hop between the molecular orbitals once they are injected from the electrode and reach the other electrode. The present work can be beneficial to overcome the "electrical short-circuit", a main drawback of MJs regarding technological issues, and offers a platform to utilize coordination compounds and organometallic compounds for electronic and optoelectronic applications.

ASSOCIATED CONTENT

Data Availability Statement

The authors declare no conflict of interest to this work.

Ⓢ Supporting Information

The Supporting Information is available free of charge at https://pubs.acs.org/doi/10.1021/acs.nanolett.3c03256.

Synthesis of 5-amino-1,10-phenanthroline and [Ru-(Phen-NH$_2$)$_3$]PF$_6$, ^{1}H NMR, FT-IR, UV−vis, and electrochemical data, fabrication of patterned ITO, electrochemical grafting, thin films characterization via AFM, XPS, electrical characterization, equivalent circuit model, and computational data (PDF)

AUTHOR INFORMATION

Corresponding Author

Prakash Chandra Mondal − *Department of Chemistry, Indian Institute of Technology Kanpur, Kanpur, Uttar Pradesh 208016, India;* ⓘ orcid.org/0000-0002-9415-5147; Email: pcmondal@iitk.ac.in

Authors

Ritu Gupta − *Department of Chemistry, Indian Institute of Technology Kanpur, Kanpur, Uttar Pradesh 208016, India;* ⓘ orcid.org/0000-0001-9026-4314

Shapath Bhandari − *Department of Chemistry, Indian Institute of Technology Kanpur, Kanpur, Uttar Pradesh 208016, India;* ⓘ orcid.org/0009-0001-8786-4834

Savas Kaya − *Department of Pharmacy, Faculty of Science, Cumhuriyet University, Sivas 58140, Turkey;* ⓘ orcid.org/0000-0002-0765-9751

Konstantin P. Katin − *Institute of Nanotechnologies in Electronics, Spintronics and Photonics, National Research Nuclear University "MEPhI", Moscow 115409, Russia;* ⓘ orcid.org/0000-0003-0225-5712

Complete contact information is available at:
https://pubs.acs.org/10.1021/acs.nanolett.3c03256

Notes

The authors declare no competing financial interest.

REFERENCES

(1) Gupta, R.; Fereiro, J. A.; Bayat, A.; Pritam, A.; Zharnikov, M.; Mondal, P. C. Nanoscale Molecular Rectifiers. *Nat. Rev. Chem.* **2023**, *7* (2), 106−122.

(2) Su, T. A.; Neupane, M.; Steigerwald, M. L.; Venkataraman, L.; Nuckolls, C. Chemical Principles of Single-Molecule Electronics. *Nat. Rev. Mater.* **2016**, *1* (3), 16002.

(3) Dief, E. M.; Low, P. J.; Díez-Pérez, I.; Darwish, N. Advances in Single-Molecule Junctions as Tools for Chemical and Biochemical Analysis. *Nat. Chem.* **2023**, *15* (5), 600−614.

(4) Van Dyck, C.; Ratner, M. A. Molecular Rectifiers: A New Design Based on Asymmetric Anchoring Moieties. *Nano Lett.* **2015**, *15* (3), 1577−1584.

(5) Zang, Y.; Stone, I.; Inkpen, M. S.; Ng, F.; Lambert, T. H.; Nuckolls, C.; Steigerwald, M. L.; Roy, X.; Venkataraman, L. In Situ Coupling of Single Molecules Driven by Gold-Catalyzed Electrooxidation. *Angew. Chem.* **2019**, *131* (45), 16154−16158.

(6) Venkataraman, L.; Klare, J. E.; Nuckolls, C.; Hybertsen, M. S.; Steigerwald, M. L. Dependence of Single-Molecule Junction Conductance on Molecular Conformation. *Nature* **2006**, *442* (7105), 904−907.

(7) Ranganathan, S.; Steidel, I.; Anariba, F.; McCreery, R. L. Covalently Bonded Organic Monolayers on a Carbon Substrate: A New Paradigm for Molecular Electronics. *Nano Lett.* **2001**, *1* (9), 491−494.

(8) Obersteiner, V.; Huhs, G.; Papior, N.; Zojer, E. Unconventional Current Scaling and Edge Effects for Charge Transport through Molecular Clusters. *Nano Lett.* **2017**, *17* (12), 7350−7357.

(9) Vilan, A.; Cahen, D. Chemical Modification of Semiconductor Surfaces for Molecular Electronics. *Chem. Rev.* **2017**, *117* (5), 4624−4666.

(10) Xie, Z.; Bâldea, I.; Frisbie, C. D. Energy Level Alignment in Molecular Tunnel Junctions by Transport and Spectroscopy: Self-Consistency for the Case of Alkyl Thiols and Dithiols on Ag, Au, and Pt Electrodes. *J. Am. Chem. Soc.* **2019**, *141* (45), 18182−18192.

(11) Kang, H.; Cho, S. J.; Kong, G. D.; Yoon, H. J. Li-Ion Intercalation, Rectification, and Solid Electrolyte Interphase in Molecular Tunnel Junctions. *Nano Lett.* **2022**, *22* (12), 4956−4962.

(12) Nguyen, Q. V.; Thi, H. L.; Truong, G. L. Chemical Conformation Induced Transport Carrier Switching in Molecular Junction Based on Carboxylic-Terminated Thiol Molecules. *Nano Lett.* **2022**, *22* (24), 10147−10153.

(13) Mondal, P. C.; Tefashe, U. M.; McCreery, R. L. Internal Electric Field Modulation in Molecular Electronic Devices by Atmosphere and Mobile Ions. *J. Am. Chem. Soc.* **2018**, *140* (23), 7239−7247.

(14) McCreery, R. L. Carbon-Based Molecular Junctions for Practical Molecular Electronics. *Acc. Chem. Res.* **2022**, *55* (19), 2766−2779.

(15) Garner, M. H.; Li, H.; Chen, Y.; Su, T. A.; Shangguan, Z.; Paley, D. W.; Liu, T.; Ng, F.; Li, H.; Xiao, S.; Nuckolls, C.; Venkataraman, L.; Solomon, G. C. Comprehensive Suppression of

Single-Molecule Conductance Using Destructive σ-Interference. *Nature* **2018**, *558* (7710), 415−419.

(16) Bruot, C.; Hihath, J.; Tao, N. Mechanically Controlled Molecular Orbital Alignment in Single Molecule Junctions. *Nat. Nanotechnol.* **2012**, *7* (1), 35−40.

(17) Yuan, L.; Nerngchamnong, N.; Cao, L.; Hamoudi, H.; del Barco, E.; Roemer, M.; Sriramula, R. K.; Thompson, D.; Nijhuis, C. A. Controlling the Direction of Rectification in a Molecular Diode. *Nat. Commun.* **2015**, *6* (1), 6324.

(18) Qiu, X.; Ivasyshyn, V.; Qiu, L.; Enache, M.; Dong, J.; Rousseva, S.; Portale, G.; Stöhr, M.; Hummelen, J. C.; Chiechi, R. C. Thiol-Free Self-Assembled Oligoethylene Glycols Enable Robust Air-Stable Molecular Electronics. *Nat. Mater.* **2020**, *19* (3), 330−337.

(19) Najarian, A. M.; McCreery, R. L. Long-Range Activationless Photostimulated Charge Transport in Symmetric Molecular Junctions. *ACS Nano* **2019**, *13* (1), 867−877.

(20) Saxena, S. K.; Tefashe, U. M.; McCreery, R. L. Photostimulated Near-Resonant Charge Transport over 60 Nm in Carbon-Based Molecular Junctions. *J. Am. Chem. Soc.* **2020**, *142* (36), 15420−15430.

(21) Bayat, A.; Lacroix, J.-C.; McCreery, R. L. Control of Electronic Symmetry and Rectification through Energy Level Variations in Bilayer Molecular Junctions. *J. Am. Chem. Soc.* **2016**, *138* (37), 12287−12296.

(22) Tuccitto, N.; Ferri, V.; Cavazzini, M.; Quici, S.; Zhavnerko, G.; Licciardello, A.; Rampi, M. A. Highly Conductive ∼ 40-Nm-Long Molecular Wires Assembled by Stepwise Incorporation of Metal Centres. *Nat. Mater.* **2009**, *8* (1), 41−46.

(23) van Nguyen, Q.; Tefashe, U.; Martin, P.; Della Rocca, M. L.; Lafolet, F.; Lafarge, P.; McCreery, R. L.; Lacroix, J. Molecular Signature and Activationless Transport in Cobalt-Terpyridine-Based Molecular Junctions. *Adv. Electron. Mater.* **2020**, *6* (7), 1901416.

(24) Balzani, V.; Juris, A. Photochemistry and Photophysics of Ru(II)-Polypyridine Complexes in the Bologna Group. From Early Studies to Recent Developments. *Coord. Chem. Rev.* **2001**, *211* (1), 97−115.

(25) Weinberg, D. R.; Gagliardi, C. J.; Hull, J. F.; Murphy, C. F.; Kent, C. A.; Westlake, B. C.; Paul, A.; Ess, D. H.; McCafferty, D. G.; Meyer, T. J. Proton-Coupled Electron Transfer. *Chem. Rev.* **2012**, *112* (7), 4016−4093.

(26) Mondal, P. C.; Singh, V.; Jeyachandran, Y. L.; Zharnikov, M. Surface-Confined Heterometallic Triads on the Basis of Terpyridyl Complexes and Design of Molecular Logic Gates. *ACS Appl. Mater. Interfaces* **2015**, *7* (16), 8677−8686.

(27) Singh, V.; Mondal, P. C.; Singh, A. K.; Zharnikov, M. Molecular Sensors Confined on SiOx substrates. *Coord. Chem. Rev.* **2017**, *330*, 144−163.

(28) Tefashe, U. M.; Nguyen, Q. V.; Lafolet, F.; Lacroix, J.-C.; McCreery, R. L. Robust Bipolar Light Emission and Charge Transport in Symmetric Molecular Junctions. *J. Am. Chem. Soc.* **2017**, *139* (22), 7436−7439.

(29) Tefashe, U. M.; Nguyen, Q. V.; Morteza Najarian, A.; Lafolet, F.; Lacroix, J.-C.; McCreery, R. L. Orbital Control of Long-Range Transport in Conjugated and Metal-Centered Molecular Electronic Junctions. *J. Phys. Chem. C* **2018**, *122* (50), 29028−29038.

(30) Terada, K.; Kanaizuka, K.; Iyer, V. M.; Sannodo, M.; Saito, S.; Kobayashi, K.; Haga, M. Memory Effects in Molecular Films of Free-Standing Rod-Shaped Ruthenium Complexes on an Electrode. *Angew. Chemie Int. Ed.* **2011**, *50* (28), 6287−6291.

(31) Atesci, H.; Kaliginedi, V.; Celis Gil, J. A.; Ozawa, H.; Thijssen, J. M.; Broekmann, P.; Haga, M.; van der Molen, S. J. Humidity-Controlled Rectification Switching in Ruthenium-Complex Molecular Junctions. *Nat. Nanotechnol.* **2018**, *13* (2), 117−121.

(32) Qu, T.-Y.; Sun, Y.; Chen, M.-L.; Liu, Z.; Zhu, Q.-B.; Wang, B.; Zhao, T.-Y.; Liu, C.; Tan, J.; Qiu, S.; Li, Q.-W.; Han, Z.; Wang, W.; Cheng, H.-M.; Sun, D.-M. A Flexible Carbon Nanotube Sen-Memory Device. *Adv. Mater.* **2020**, *32* (9), 1907288.

(33) Farquhar, A. K.; Supur, M.; Smith, S. R.; Van Dyck, C.; McCreery, R. L. Hybrid Graphene Ribbon/Carbon Electrodes for High-Performance Energy Storage. *Adv. Energy Mater.* **2018**, *8* (35), 1802439.

(34) Karipidou, Z.; Branchi, B.; Sarpasan, M.; Knorr, N.; Rodin, V.; Friederich, P.; Neumann, T.; Meded, V.; Rosselli, S.; Nelles, G.; Wenzel, W.; Rampi, M. A.; von Wrochem, F. Ultrarobust Thin-Film Devices from Self-Assembled Metal-Terpyridine Oligomers. *Adv. Mater.* **2016**, *28* (18), 3473−3480.

(35) Yao, X.; Sun, X.; Lafolet, F.; Lacroix, J.-C. Long-Range Charge Transport in Diazonium-Based Single-Molecule Junctions. *Nano Lett.* **2020**, *20* (9), 6899−6907.

(36) Gupta, R.; Pradhan, J.; Haldar, A.; Murapaka, C.; Mondal, P. C. Chemical Approach Towards Broadband Spintronics on Nanoscale Pyrene Films. *Angew. Chemie Int. Ed.* **2023**, *62* (35), e202307458.

(37) Dief, E. M.; Vogel, Y. B.; Peiris, C. R.; Le Brun, A. P.; Gonçales, V. R.; Ciampi, S.; Reimers, J. R.; Darwish, N. Covalent Linkages of Molecules and Proteins to Si-H Surfaces Formed by Disulfide Reduction. *Langmuir* **2020**, *36* (49), 14999−15009.

(38) Pinson, J.; Podvorica, F. I. Surface Modification of Materials: Electrografting of Organic Films. *Curr. Opin. Electrochem.* **2020**, *24* (v), 44−48.

(39) de Ruiter, G.; Lahav, M.; van der Boom, M. E. Pyridine Coordination Chemistry for Molecular Assemblies on Surfaces. *Acc. Chem. Res.* **2014**, *47* (12), 3407−3416.

(40) Maeda, H.; Sakamoto, R.; Nishihara, H. Interfacial Synthesis of Electrofunctional Coordination Nanowires and Nanosheets of Bis(Terpyridine) Complexes. *Coord. Chem. Rev.* **2017**, *346*, 139−149.

(41) Ding, X.; Xue, J.; Ding, S.; Chen, C.; Wang, X.; Yu, X.; Hu, W. Bi-polaron Transport and Magnetic Field Induced Pauli Spin Blockade in Redox-Active Molecular Junctions. *Angew. Chemie Int. Ed.* **2022**, *61* (44), e202208969.

(42) Akkerman, H. B.; Naber, R. C. G.; Jongbloed, B.; van Hal, P. A.; Blom, P. W. M.; de Leeuw, D. M.; de Boer, B. Electron Tunneling through Alkanedithiol Self-Assembled Monolayers in Large-Area Molecular Junctions. *Proc. Natl. Acad. Sci. U. S. A.* **2007**, *104* (27), 11161−11166.

(43) Yan, H.; Bergren, A. J.; McCreery, R.; Della Rocca, M. L.; Martin, P.; Lafarge, P.; Lacroix, J. C. Activationless Charge Transport across 4.5 to 22 Nm in Molecular Electronic Junctions. *Proc. Natl. Acad. Sci. U. S. A.* **2013**, *110* (14), 5326−5330.

(44) Pillonnet, A.; Ongaro, R. Synthetic Representations of the Poole Frenkel (PF) and Poole Regimes. *Rev. Phys. Appliquée* **1990**, *25* (2), 229−242.

(45) Dias, S.; Murali, B.; Krupanidhi, S. B. Transport Properties of Solution Processed Cu2SnS3/AZnO Heterostructure for Low Cost Photovoltaics. *Sol. Energy Mater. Sol. Cells* **2015**, *143*, 152−158.

(46) Nguyen, Q. V.; Martin, P.; Frath, D.; Della Rocca, M. L.; Lafolet, F.; Bellinck, S.; Lafarge, P.; Lacroix, J. C. Highly Efficient Long-Range Electron Transport in a Viologen-Based Molecular Junction. *J. Am. Chem. Soc.* **2018**, *140* (32), 10131−10134.

(47) Jash, P.; Parashar, R. K.; Fontanesi, C.; Mondal, P. C. The Importance of Electrical Impedance Spectroscopy and Equivalent Circuit Analysis on Nanoscale Molecular Electronic Devices. *Adv. Funct. Mater.* **2022**, *32* (10), 2109956.

(48) Giannozzi, P.; Andreussi, O.; Brumme, T.; Bunau, O.; Buongiorno Nardelli, M.; Calandra, M.; Car, R.; Cavazzoni, C.; Ceresoli, D.; Cococcioni, M.; Colonna, N.; Carnimeo, I.; Dal Corso, A.; de Gironcoli, S.; Delugas, P.; DiStasio, R. A.; Ferretti, A.; Floris, A.; Fratesi, G.; Fugallo, G.; Gebauer, R.; Gerstmann, U.; Giustino, F.; Gorni, T.; Jia, J.; Kawamura, M.; Ko, H.-Y.; Kokalj, A.; Küçükbenli, E.; Lazzeri, M.; Marsili, M.; Marzari, N.; Mauri, F.; Nguyen, N. L.; Nguyen, H.-V.; Otero-de-la-Roza, A.; Paulatto, L.; Poncé, S.; Rocca, D.; Sabatini, R.; Santra, B.; Schlipf, M.; Seitsonen, A. P.; Smogunov, A.; Timrov, I.; Thonhauser, T.; Umari, P.; Vast, N.; Wu, X.; Baroni, S. Advanced Capabilities for Materials Modelling with Quantum ESPRESSO. *J. Phys.: Condens. Matter* **2017**, *29* (46), 465901.

(49) Giannozzi, P.; Baseggio, O.; Bonfà, P.; Brunato, D.; Car, R.; Carnimeo, I.; Cavazzoni, C.; de Gironcoli, S.; Delugas, P.; Ferrari Ruffino, F.; Ferretti, A.; Marzari, N.; Timrov, I.; Urru, A.; Baroni, S.

Quantum ESPRESSO toward the Exascale. *J. Chem. Phys.* **2020**, *152* (15), 154105.

(50) Brewer, S. H.; Franzen, S. Calculation of the Electronic and Optical Properties of Indium Tin Oxide by Density Functional Theory. *Chem. Phys.* **2004**, *300* (1−3), 285−293.

(51) Calixto, M.; Maldonado, D.; Miranda, E.; Roldán, J. B. Modeling of the Temperature Effects in Filamentary-Type Resistive Switching Memories Using Quantum Point-Contact Theory. *J. Phys. D. Appl. Phys.* **2020**, *53* (29), 295106.